Case Studies in Thermal Engineering 85 (2026) 108371

Contents lists available at ScienceDirect

Case Studies in Thermal Engineering

journal homepage: www.elsevier.com/locate/csite

Gradient porosity copper foam for enhancing heat transfer efficiency and energy output density of OTEC thermal engine: An experimental and numerical study

Zengbao Zhang [a], Wenzhuo Shi [a], Sihan Zhang [a], Jingzhi Zhang [b], Bingzhen Wang [c], Shizhen Li [a,*]

[a] Institute of Marine Science and Technology, Shandong University, Qingdao, PR China
[b] School of Energy and Power Engineering, Shandong University, Jinan, PR China
[c] National Ocean Technology Center, Tianjin, PR China

GRAPHICAL ABSTRACT

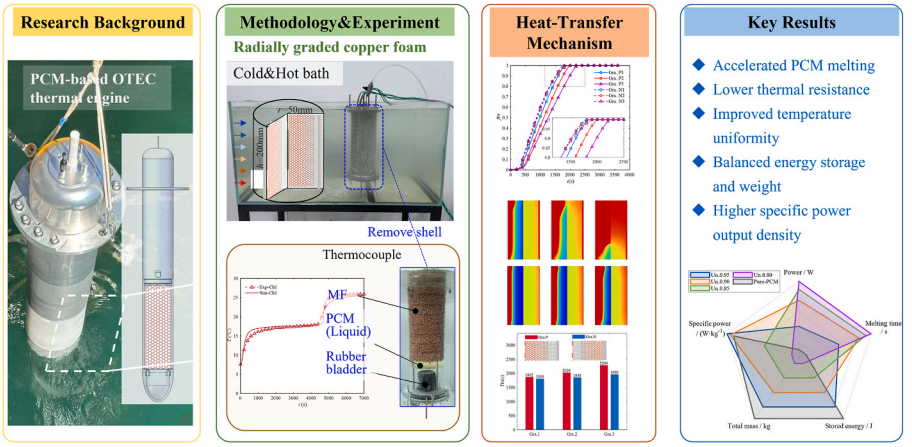

ARTICLE INFO

Keywords:
OTEC thermal engine
Metal foam

ABSTRACT

Ocean thermal energy conversion (OTEC) thermal engine have the advantage of providing continuous power and are therefore regarded as an attractive energy source for underwater vehicles. However, their operating frequency was constrained by the inherently low melting rate of

* Corresponding author.
E-mail address: lishizhen@sdu.edu.cn (S. Li).

https://doi.org/10.1016/j.csite.2026.108371
Received 6 March 2026; Received in revised form 5 July 2026; Accepted 20 July 2026
Available online 21 July 2026

Gradient porosity
Phase change material
Melting rate

the internal phase change material (PCM). Conventional enhancement using metal foam could accelerate PCM melting, but it markedly increased the structural weight of the device and could even lead to higher parasitic energy consumption. To address this challenge, the present study investigated a radially layered porosity strategy for copper foam. Through combined experiments and numerical simulations, the temporal and spatial evolution of liquid fraction and temperature under different gradient directions and gradient magnitudes was examined, and the temperature uniformity, power output, and power-to-weight performance were evaluated. The results showed that a lower porosity led to a faster melting rate; specifically, the copper-foam configuration with a porosity of 0.8 reduced the complete melting time by 48.7% compared with pure PCM. Both positive and negative graded configurations improved the temperature uniformity by 15.4–42.4%. Finally, although the low-porosity layer provided a higher effective thermal conductivity, it weakened natural convection and thereby suppressed the melting process, whereas a moderate positive porosity gradient maintained a balance between self-weight and thermal performance. This work thus offered useful insights for the development of high–power-density OTEC thermal engine.

Nomenclature

Abbreviations		$S_x S_y$	source terms
OTEC	ocean thermal energy conversion	t	time(s)
PCM	phase change material	t_m	total melting time(s)
MF	metal foam	T	temperature(°C)
		V_{PCM}	volume of the PCM volume
Gra.N	negative porosity gradient	U	Velocity(m/s)
Gra.P	positive porosity gradient	V	volume(m^3)
PPI	pores per inch	**Greek symbols**	
Symbols		a_{sf}	interfacial surface area per unit volume($1/m$)
A_{mush}	mushy-zone constant	β	thermal expansion coefficient of PCM(1/K)
c_p	specific heat capacity ($J/(kg \cdot K)$)	ε	porosity
C_i	inertia coefficient	λ	thermal conductivity($W/(m \cdot K)$)
d_l	effective pore length(m)	μ	dynamic viscosity (Pa s)
d_p	equivalent pore size size(m)	ρ	density(kg/m^3)
E	energy density(W/kg)	σ_m	time-averaged RMS temperature difference(°C)
f_m	liquid fraction	σ	transient RMS temperature difference(°C)
g	gravitational acceleration(m/s2)	ω	pore density parameter
h_{sf}	interfacial heat transfer coefficient($W/m^{-2} \cdot K^{-1}$)	τ	normalized melting progress
K	permeability(m^2)	**Subscripts**	
L	latent heat(J/kg)	cf	copper foam
P	storage power	e	effective
		l	liquid phase
p	pressure(Pa)	max	maximum value
$\overline{p_a}$	average pressure in the accumulator(Pa)	pcm	phase change material
Pr	Prandtl number	s	solid phase
Ra_d	Rayleigh number	x, y	spatial coordinates

1. Introduction

Profiling floats and underwater gliders have become important platforms for long-duration ocean observation, marine resource exploration, environmental monitoring, and military applications [1–3]. Their endurance, however, remains strongly constrained by the limited onboard energy supply. Ocean thermal energy conversion (OTEC) provides an attractive solution for underwater vehicles because it can harvest the naturally existing temperature difference between warm surface seawater and cold deep seawater. Compared with conventional batteries, an OTEC-based power system has the potential to provide repeated and in-situ energy replenishment during vertical profiling motion. In such systems, PCM-based thermal engines are particularly promising because solid–liquid phase change can convert ocean thermal energy into mechanical or hydraulic energy through volumetric expansion [4–6] For PCM-based OTEC thermal engines, the phase-change process inside the heat-exchange/storage chamber directly governs the thermal response and energy-output capability. When the vehicle ascends into the warm surface layer, the PCM absorbs heat and melts; the associated volume expansion drives hydraulic oil into an accumulator, where the absorbed thermal energy is stored in mechanical form. The response rate of this process determines the charging rate of the accumulator, the operating frequency of the thermal engine, and ultimately the mission endurance of the underwater vehicle. Although alkane-based PCMs possess suitable phase-change temperatures and relatively large volume expansion, their inherently low thermal conductivity severely limits heat absorption and release. As a result, melting and solidification proceed slowly, leading to a long thermal-cycle time and a reduced energy-output rate.

Various heat-transfer enhancement methods have been explored to overcome the low thermal conductivity of PCMs. Nanoparticle addition is one widely used approach. For example, Şahan et al. [7] improved the thermal conductivity of paraffin by adding

nano-magnetic iron oxide, Singh et al. [8] developed graphite-foam/$MgCl_2$ composites for latent heat storage, and Harikrishnan et al. [9] showed that Al_2O_3 nanoparticles can reduce the melting time of PCM. Nevertheless, nanoparticle-enhanced PCMs may suffer from agglomeration, sedimentation, saturation of enhancement effects, and long-term stability issues during repeated thermal cycling [10]. Fins provide another effective pathway for increasing the heat-transfer area and reducing thermal resistance. Li et al. [11]introduced fins into an ocean thermal energy storage unit and reported an improved storage efficiency. However, fins occupy PCM volume, increase system weight, and may suppress local natural convection when the fin density [12] or geometric blockage becomes excessive [13,14]. These limitations are particularly important for underwater vehicles, where both thermal response and mass penalty must be carefully controlled.

Metal foams have attracted considerable attention because they provide a continuous high-conductivity skeleton inside the PCM while maintaining interconnected pores for liquid PCM motion [15–17]. By embedding metal foam into PCM, the effective thermal conductivity can be significantly increased, and the melting front can propagate more rapidly than in pure PCM. Recent studies have further shown that the performance of PCM–metal foam composites is sensitive to the arrangement of flow channels, heating elements, porous structures, and charging/discharging modes [18–23]. Wei et al. [24] investigated heat transfer in composite PCMs with uniform porosity, while Zhang et al. [25] numerically investigated the energy storage characteristics of cuboid aluminum foam and found that when the porosity exceeds 91.3%, the energy storage density is positively correlated with the equivalent porosity during phase change. They further pointed out that configurations with a positive porosity gradient outperform those with a negative gradient. Si et al. [26] showed that the total melting time of the PCM can be shortened by an appropriately designed linear porosity gradient, and the average power density can be enhanced by about 15.8% when compared with a uniform-porosity structure. Zhao et al. [27] experimentally showed that the heat transfer rate can be significantly enhanced by embedding copper foam with a graded pore distribution into paraffin; furthermore, with an optimized pore structure, the maximum temperature difference was reduced by approximately 71.4%, and a much more uniform PCM temperature field was obtained.

These findings indicate that metal-foam enhancement is not governed solely by the increase in effective thermal conductivity, but also by the spatial distribution of pore space and flow resistance. Metal foams with graded porosity have thus been proposed as an improved solution to reconcile energy storage density and heat transfer performance [28]. By redistributing the high-conductivity metal skeleton and the liquid-flow passages within the PCM domain, graded foams provide an additional degree of freedom for regulating the competition between conduction enhancement and natural convection. According to Venkateshwar [29], although smaller morphological parameters are associated with a higher average heat transfer efficiency during the early stages of solidification, the relationship reverses as solidification proceeds, and an opposite trend is observed in the later stages. Lafdi et al. [30] experimentally found that high-porosity composites exhibit higher heat transfer efficiency, attributing this to the fact that lower porosity induces larger flow resistance and suppresses natural convection in the PCM. Consistently, the results of Zhu et al. [31] also indicate that lower porosity does not necessarily guarantee superior overall performance.

These studies have clarified important heat-transfer mechanisms in metal-foam/PCM composites, especially the trade-off among effective thermal conductivity, permeability, natural convection, and PCM volume fraction. Nevertheless, most existing studies on graded metal-foam/PCM systems have been developed for conventional latent heat storage units, such as cuboid storage modules, annular enclosures, shell-and-tube systems, or generalized thermal management devices. Accordingly, their performance evaluations have mainly focused on thermal indicators. These indicators are essential for conventional thermal-storage applications, but they do not fully reflect the application-specific requirements of PCM-based OTEC thermal engines. In an OTEC thermal engine, the PCM is not only a thermal storage medium; its melting-induced volumetric expansion is also used to drive hydraulic oil into an accumulator, thereby converting absorbed ocean thermal energy into mechanical energy. Therefore, a graded-porosity configuration that shortens the melting time may not necessarily be optimal if it introduces excessive metal-foam mass, reduces the available PCM volume, weakens liquid-PCM motion, or lowers the mass-specific power output of the underwater vehicle. From this perspective, the design of

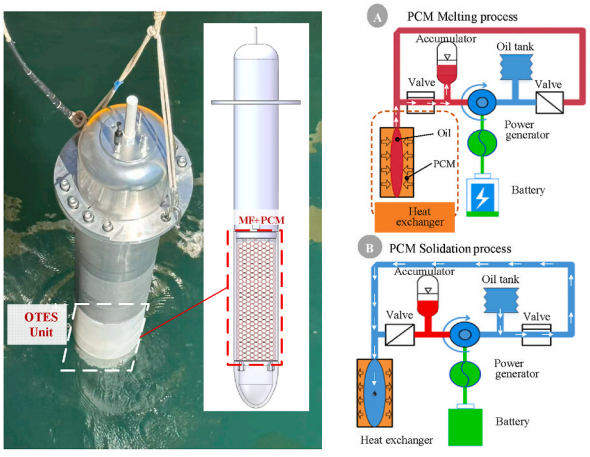

Fig. 1. Working principle of OTEC engine.

graded metal foam for OTEC thermal engines requires an OTEC-oriented evaluation framework that couples melting behavior, temperature uniformity, mechanical energy storage, structural mass, and power-to-weight performance.

Motivated by these application-specific requirements, the present study proposes a radially layered copper-foam strategy for the PCM heat-exchange/storage chamber of an OTEC thermal engine. As schematically illustrated in Fig. 1, the working principle of the OTEC system is established by coupling the temperature-stratified ocean environment with a PCM-based storage-and-conversion process. When the profiler ascends into the warm surface layer, PCM melting accompanied by volumetric expansion is triggered, which drives hydraulic oil into an accumulator so that the absorbed ocean thermal energy is ultimately stored in mechanical form. In this work, numerical simulations are performed to compare the thermal performance of a thermal storage unit configured as PCM filled with uniform-porosity copper foam, and PCM filled with various radially graded-porosity copper foams, thereby enabling a consistent evaluation across representative structural configurations. In the present OTEC thermal engine, PCM melting is accompanied by volume expansion, which drives hydraulic oil into the accumulator and directly determines the energy-storage rate and output power. Therefore particular attention is paid to the extent to which the porosity gradient profile and the gradient magnitude govern the PCM melting rate, temperature distribution, and specific power output density during the heat-absorption stage. The present study focuses on the melting process as the primary stage for evaluating the proposed graded-porosity strategy.

2. Experimental design

2.1. Experiment system

As illustrated in Fig. 2, the experimental system consists of a heating and cooling machine and a circulating water tank that provide controlled thermal boundary conditions, together with the OTEC heat-engine module instrumented by sensors and data acquisition devices. The water bath is employed to reproduce the temperature difference between the surface and deep seawater so that the operating thermal conditions relevant to the OTEC heat engine can be represented in a controlled manner. The metal-foam (MF) structure of the module was filled with n-hexadecane as the phase change material (PCM), with the corresponding thermophysical properties listed Table 1. A rubber bladder located beneath the module is filled with hydraulic oil. The oil-measurement cylinder connected to the bladder records the volumetric changes during the phase transition via a displacement sensor, enabling identification of the phase-change progress. Meanwhile, the temperature evolution over the entire phase transition process is recorded by K-type thermocouples to enable a continuous characterization of phase-transition progression.

According to previous study [11], in the operational region of the OTEC thermal engine, the surface seawater temperature typically lies between 23 and 27 °C, whereas the deep cold seawater temperature is generally in the range of 4–8 °C, constant water-bath temperatures of 8 °C and 26 °C are maintained for the cold and hot modes, respectively. The temperature measurement point is located at (r/2, h/2). The OTEC heat engine was initially placed in a cold water tank before the experiment started, so that a controlled solidification state could be established prior to subsequent heating. When the temperature measured by the internal thermocouple became stable and approached the external water temperature, it was considered to be completely solidified, and the zero point of the displacement of the phase change cylinder was recorded. Then the heat engine was moved to a hot water tank. The PCM melted and expanded when heated, pushing the piston rod of the measuring cylinder to extend. When the displacement stopped rising and the temperature of the internal thermocouple was consistent with the external water temperature, it was regarded as completely melted. The sampling interval of temperature data was set to 1 s.

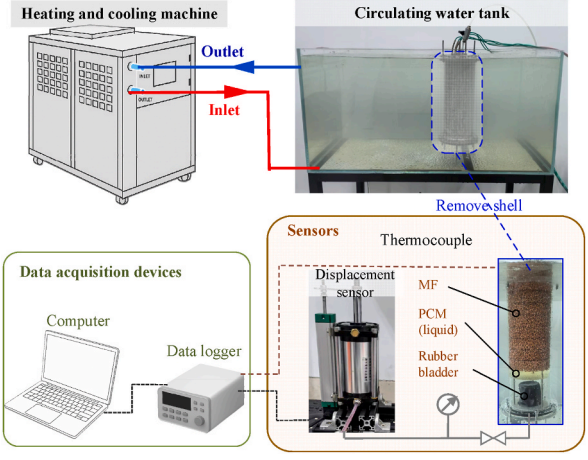

Fig. 2. Experimental system.

Table 1
Thermo-physical properties of materials used in this study.

Property	n-hexadecane		Aluminium alloy	Copper
	solid	liquid		
$\rho(\mathrm{kg/m^3})$	864	776	2703	8910
$c(\mathrm{J/kg\cdot K})$	1640	2090	963	380
$\lambda(\mathrm{W/m\cdot K})$	0.313	0.14	180	400
$\mu(\mathrm{Pa\cdot s})$	/	0.0032	/	/
$T_s(\mathrm{K})$	289.15		/	/
$T_l(\mathrm{K})$	291.15		/	/
$L(\mathrm{J/kg})$	236000		/	/
$\beta(1/\mathrm{K})$	0.00089		/	/

2.2. Uncertainty analysis

The uncertainty of the experimental instruments are listed in Table 2. By accounting for the accuracy limits of both the sensors and the data acquisition system, the standard errors were determined to be ±0.876% for the liquid-fraction measurement and ±0.871% for the temperature measurement, respectively.

2.3. Experimental results

As shown in Fig. 3(a) the experimentally measured liquid fraction during melting at a porosity of 96% is compared with the data reported by Xia et al. [32]. The maximum deviation is 5.38%, indicating that the numerical results fall within a reasonable error range. Fig. 3 (b) compares the simulated and experimental temperature evolution at the central measurement point during melting for a copper foam of 0.96 porosity and 10 PPI. It can be observed that prior to the onset of phase change, the simulated temperature is slightly higher than the measured value, whereas after completion of the phase change, it becomes slightly lower. These discrepancies may be attributed to non-uniform porosity distribution of the actual metal foam and slight deviations in sensor positioning. Nevertheless, the overall melting-time trend is consistent, supporting the validity of the model for subsequent evaluation.

3. Numerical model

3.1. Governing equations

In this study, the enthalpy–porosity method is employed to simulate the phase change process [24], in which the mushy region where solid and liquid coexist is treated as a porous medium so that phase interaction can be represented within a unified formulation. For computational simplification while preserving the dominant physics, a 2D axisymmetric model is adopted. The following assumptions are adopted.

(1) The flow of liquid PCM is assumed to be incompressible and laminar;
(2) The Darcy–Brinkman model is used to describe flow resistance within the porous medium;
(3) Density variations of the PCM follow the Boussinesq approximation;
(4) The specific heat and thermal conductivity are fitted by piecewise functions and the remaining thermophysical properties are assumed constant;
(5) The copper foam and PCM are assumed to be isotropic and homogeneous.

In addition, each copper-foam layer is treated as a homogeneous and isotropic porous medium under a volume-averaged framework. The stochastic three-dimensional pore morphology is not explicitly resolved; instead, its macroscopic effects are represented by porosity-dependent permeability, inertial coefficient, interfacial area density, and effective thermal conductivity. At the interfaces between adjacent radial layers, a conformal mesh is used, and temperature and heat flux are assumed to be continuous, corresponding to an ideal thermal-contact condition.

Continuity:

$$\nabla U = 0 \tag{1}$$

Table 2
Uncertainty of the experimental instruments.

	Temperature controller/°C	Pore density/%	Thermocouple /°C	Displacement /mm	Data logger/%
Uncertainty	±0.2	±0.5	±0.2	±0.1	±0.1

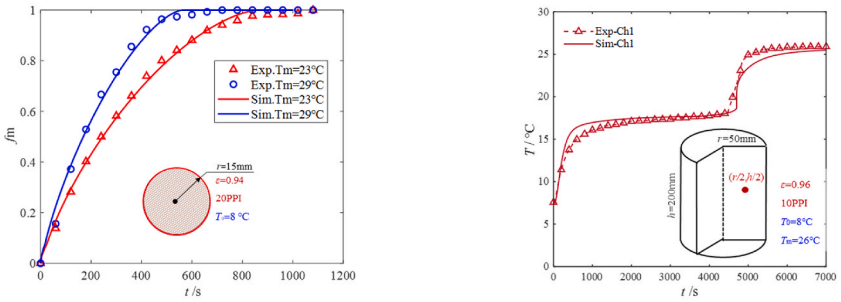

(a) Liquid fraction (b) Temperature at the measurement point

Fig. 3. Comparison between experimental and numerical results.

Momentum:

$$\frac{\rho}{\varepsilon}\left(\frac{\partial u_x}{\partial t}\right)+\frac{\rho}{\varepsilon^2}\left(u_x\cdot\nabla u_x\right)=-\nabla p+\frac{\mu}{\varepsilon}\nabla^2 u_x+S_x \tag{2}$$

$$\frac{\rho}{\varepsilon}\left(\frac{\partial u_y}{\partial \tau}\right)+\frac{\rho}{\varepsilon^2}\left(u_y\cdot\nabla u_y\right)=-\nabla p+\frac{\mu}{\varepsilon}\nabla^2 u_y+S_y \tag{3}$$

Where,

$$S_x=-A_{mush}\left(\frac{(1-f)^2}{f^3+c}\right)u_x-\frac{\mu}{K}u_x-\frac{1}{\sqrt{K}}C_i\rho u_x\sqrt{{u_x}^2+{u_y}^2} \tag{4}$$

$$S_y=-A_{mush}\left(\frac{(1-f)^2}{f^3+c}\right)u_y-\frac{\mu}{K}u_y-\frac{1}{\sqrt{K}}C_i\rho u_y\sqrt{{u_x}^2+{u_y}^2} \tag{5}$$

Here, ρ represents the density of PCM and ε represents the porosity of copper foam, and S_x, S_y denote the source terms in the momentum equations; moreover, the mushy-zone constant A_{mush} is set to 1×10^5, c is a constant term set to 0.001. The viscosity and inertial effects are related to the permeability (K). β denotes the volumetric thermal expansion coefficient of PCM [33].

Energy:

$$\varepsilon\rho_{pcm}\left(c_{p,pcm}+L\frac{df}{d\tau}\right)\frac{\partial T_p}{\partial\tau}+\rho_{pcm}c_{p,pcm}\vec{u}\nabla T_p=\nabla\left(\lambda_{e,pcm}\nabla T_p\right)+h_{sf}a_{sf}\left(T_{cf}-T_p\right) \tag{6}$$

for copper foam:

$$(1-\varepsilon)\rho_{cf}c_{p,cf}\left(\frac{\partial T_{cf}}{\partial\tau}\right)=\nabla\left(\lambda_{e,cf}\nabla T_{cf}\right)+h_{sf}a_{sf}\left(T_p-T_{cf}\right) \tag{7}$$

Where, $\lambda_{e,pcm}$ and $\lambda_{e,cf}$ represent the effective thermal conductivity of the PCM and copper foam, respectively. The pore structure parameters of copper foam are defined as the follows:

$$d_p=\frac{0.0254}{PPI}$$

$$d_l=1.18\cdot d_p\sqrt{\frac{1-\varepsilon}{3\pi}}\left(\frac{1}{1-e^{-\frac{1-\varepsilon}{0.04}}}\right)$$

The permeability and inertia coefficients are defined as the follows [34]:

$$K=0.00073(1-\varepsilon)^{-0.224\left(\frac{d_l}{d_p}\right)^{-1.11}}d_p^2 \tag{8}$$

$$C_i=0.00212(1-\varepsilon)^{-0.132\left(\frac{d_l}{d_p}\right)^{-1.63}} \tag{9}$$

According to Pourakabar [35], the effective thermal conductivity is calculated as:

$$\lambda_e = \frac{1}{\sqrt{2}(M_A + M_B + M_C + M_D)} \tag{10}$$

Where,

$$M_A = \frac{4\sigma}{(2e^2 + \pi\sigma(1-e))k_c + (4 - 2e^2 - \pi\sigma(1-e))k_p}$$

$$M_B = \frac{(e-2\sigma)^2}{(e-2\sigma)e^2k_c + (2e - 4\sigma - (e-2\sigma)e^2)k_p}$$

$$M_C = \frac{\left(\sqrt{2} - 2e\right)^2}{2\pi\sigma^2\left(1 - 2\sqrt{2}\,e\right)k_c + 2\left(\sqrt{2} - 2e - \pi\sigma^2\left(1 - 2\sqrt{2}\,e\right)\right)k_p}.$$

$$M_D = \frac{2e}{e^2k_c + (4 - e^2)k_p}$$

$$\sigma = \sqrt{\frac{\sqrt{2}\left(2 - 5/8e^3\sqrt{2} - 2\varepsilon\right)}{\pi\left(3 - 4e\sqrt{2} - e\right)}}, e = 0.339$$

Interfacial surface area per unit volume a_{sf} is defined as

$$a_{sf} = 3\pi\frac{\left(1 - e^{\frac{-1-\varepsilon}{0.04}}\right)}{\left(0.59d_p\right)^2}d_l \tag{11}$$

During melting, the liquid phase change material (PCM) flows through the pore network of the copper foam. The empirical correlation is employed to calculate the interfacial heat transfer coefficient h_{sf} [36]:

$$h_{\mathrm{sf}} = \frac{k_p}{d_l}\left[0.6 + \frac{0.387Ra_d^{1/6}}{\left[1 + \left(\frac{0.559}{Pr}\right)^{9/16}\right]^{8/27}}\right]^2 \tag{12}$$

Where, Ra_{d} denotes Rayleigh number and Pr denotes the Prandtl number.

The PCM/copper-foam composite is described as a porous medium with porosity-dependent thermophysical and flow-resistance parameters. A local thermal non-equilibrium formulation is adopted, in which the PCM and copper foam have separate temperature fields and are coupled through the interfacial heat-transfer term $h_{sf}a_{sf}\left(T_{cf} - T_{pcm}\right)$.

The phase-change process is described using the enthalpy–porosity method, and the liquid fraction is defined as:

$$f = \begin{cases} 0, T < T_s \\ \dfrac{T - T_s}{T_l - T_s}, T_s \le T \le T_l \\ 1, T > T_l \end{cases} \tag{13}$$

The boundary and initial conditions are specified as follows:

The initial state was set as a fully solidified PCM domain, with $T_{pcm} = T_{cf} = T_0$

At the solid-liquid interface, the heat flux satisfies the energy conservation, which can be mathematically expressed as:

$$T_{\mathrm{l}} = T_{\mathrm{s}} \tag{14}$$

$$-\lambda_s\left(\frac{\partial T_{\mathrm{s}}}{\partial \mathrm{n}}\right) = -\lambda_l\left(\frac{\partial T_{\mathrm{l}}}{\partial \mathrm{n}}\right) \tag{15}$$

Where λ_s, λ_l represent the thermal conductivity coefficients of the PCM in the solid phase and liquid phase, respectively.

3.2. Model independence verification

In the commercial CFD package ANSYS Fluent, the solid–liquid phase change problem is solved using the SIMPLE algorithm for pressure–velocity coupling. The PRESTO! scheme is adopted for pressure discretization, while a second-order upwind scheme is employed for the spatial discretization of the momentum and energy equations. The convergence criteria for the residuals of the continuity, momentum, and energy equations are set to sufficiently stringent levels to 10^{-3}, 10^{-3} and 10^{-6} ensure numerical accuracy.

The melting process of the PCM with a uniformly porous metal foam $\varepsilon = 0.96$ was examined under different grid resolutions, with cell counts of 28604, 46248, 74358, 176382, and 286354, respectively. As shown in Fig. 4(a), the total melting time was evaluated for time steps of 0.02 s, 0.05 s, 0.1 s, 0.2 s, and 0.3 s. It can be seen that a time step of 0.1 s is able to accurately capture the melting process while maintaining acceptable computational efficiency. Fig. 4 (b) presents the total melting time for different mesh sizes, from which it is observed that a mesh with 176,382 cells already yields sufficiently grid-independent results. Therefore, a mesh containing 176382 cells and a time step of 0.1 s are adopted in all subsequent simulations.

4. Results and discussions

4.1. Effect of different uniform porosity

Fig. 5 compares the evolution of the liquid fraction with time for structures with different uniform porosities. The results indicate that, in the early stage of melting, the increase in liquid fraction is similar for all cases. However, in the middle and late stages of melting, the liquid fraction for low-porosity configurations approaches unity much more rapidly, whereas high-porosity configurations exhibit a pronounced delay. This discrepancy can be attributed to the fact that the initial melting process is dominated by thermal conduction. This trend indicates that the effect of porosity is more pronounced after a sufficient liquid layer has formed. In the early stage, melting is mainly controlled by heat conduction near the heated wall, whereas in the middle and late stages the copper skeleton provides additional heat-transfer paths and accelerates the inward movement of the melting front.

Fig. 6 compares the total melting time for each configuration. Relative to the case without foam, filling the cavity with copper foam markedly shortens the melting duration: for configuration 1, the total melting time is reduced by 30.5%. As the porosity is further decreased by each additional 5%, the total melting time is reduced by 755 s, 382 s, and 262 s, respectively. The decreasing reduction in melting time suggests a saturation tendency of conductive enhancement. Although a lower porosity increases the effective thermal conductivity, it also reduces permeability and weakens liquid PCM circulation; therefore, further porosity reduction does not lead to a proportional improvement in melting rate.

To elucidate the spatial discrepancies induced by different porosity configurations, Fig. 7 compares the liquid fraction field (left) and temperature field (right) at 500 s, 1000 s, 1500 s, 2000 s, and 2500 s. In all configurations, the solid–liquid interface is nearly vertical before 500 s. After 500 s, as melting proceeds, the melting efficiency is significantly enhanced by the insertion of copper foam. The melted liquid PCM is driven upward by buoyancy, causing the upper part of the solid–liquid interface to bulge toward the PCM region, which indicates that heat accumulates near the upper zone and then starts to propagate inward and downward. At the early melting stage, heat is mainly conducted from the heated wall to the solid PCM. Once the liquid phase appears, the density difference between solid and liquid phases gives rise to buoyancy-driven flow, and the liquid PCM undergoes natural convection. In the later stage of melting, the temperature field becomes nearly symmetric with the liquid fraction field, suggesting that a lower porosity suppresses natural convection, so that heat transfer is dominated by conduction, leading to a reduction in the melting rate. The deformation of the melting front reflects the onset of buoyancy-driven liquid PCM motion after the formation of a liquid layer. For lower-porosity foams, this deformation becomes less evident because the porous skeleton imposes stronger flow resistance, causing heat transfer to become more conduction-dominated. This trend is also consistent with the results shown in Fig. 5.

To characterize the spatial temperature uniformity, Eqs. (15) and (16) are introduced to quantify the root-mean-square (RMS) temperature difference[37] between monitoring points and its corresponding time-averaged value.

$$\sigma(t) = \sqrt{\frac{\sum_{i=1}^{n} (T(i) - T_{mean})^2}{n}} \tag{16}$$

$$\sigma_{\mathrm{m}} = \sum_{i=1}^{n} \sigma(t) \Big/ \mathrm{n} \tag{17}$$

Fig. 8 presents the evolution of temperature non-uniformity for different porosities. It can be observed that, over the entire melting

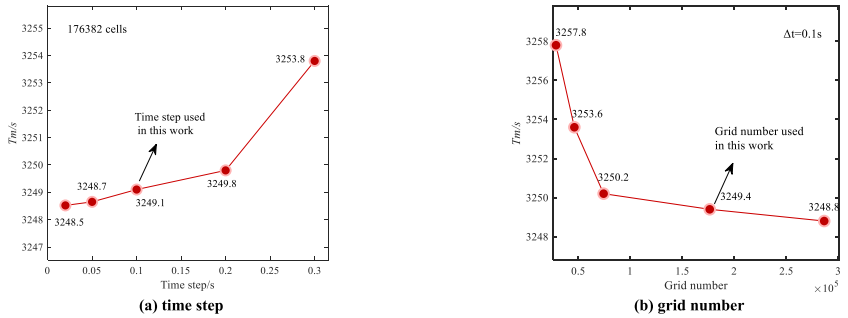

Fig. 4. Grid and time step independence analysis.

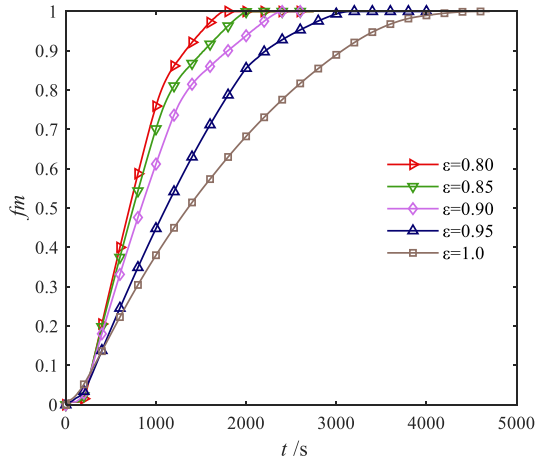

Fig. 5. Evolution of the liquid fraction for different uniform porosity.

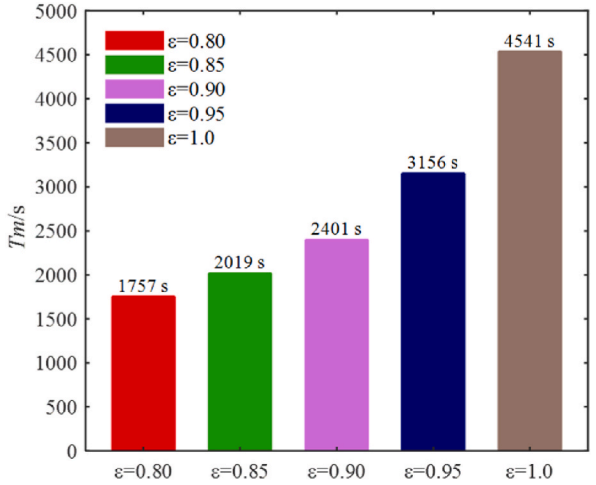

Fig. 6. Comparison of total melting time for different uniform porosity.

period, the σ_m generally decreases with decreasing porosity. For all configurations, the curves exhibit two distinct stages of "first increasing and then decreasing": the initial rise reflects the sharp temperature increase near the heat source at the onset of melting, which aggravates temperature non-uniformity; subsequently, as liquid PCM appears, heat diffuses toward the remote regions, thereby mitigating the thermal non-uniformity. The second increase in the non-uniformity index at a later stage indicates delayed melting of PCM near the inner cold region, which increases the local thermal resistance. When the porosity is 0.8, the RMS temperature difference is 0.556 °C, lower than the value of 1.084 °C at a porosity of 0.95, implying a 48.7% improvement in temperature uniformity. The reduced temperature non-uniformity is mainly associated with the more connected copper network at lower porosity, which spreads heat from the heated side to the inner PCM region. Thus, the improvement in temperature uniformity is primarily caused by enhanced conductive heat redistribution rather than stronger natural convection.

However, due to the relatively high bulk density of copper foam, low-porosity structures, although capable of significantly shortening the melting time, inevitably increase the self-weight of the device. For an OTEC heat engine, shortening the melting time and improving the power-to-mass ratio are both crucial for enhancing the sampling frequency and energy utilization efficiency [38]. Therefore, it is necessary to introduce the storage power P and the energy density E to comprehensively evaluate the overall system:

$$P = \frac{\overline{p_a} \cdot \beta \cdot V_{PCM}}{T_m} \tag{18}$$

$$E = \frac{P}{\rho_{PCM} V_{PCM} + \rho_{MF} V_{MF}} \tag{19}$$

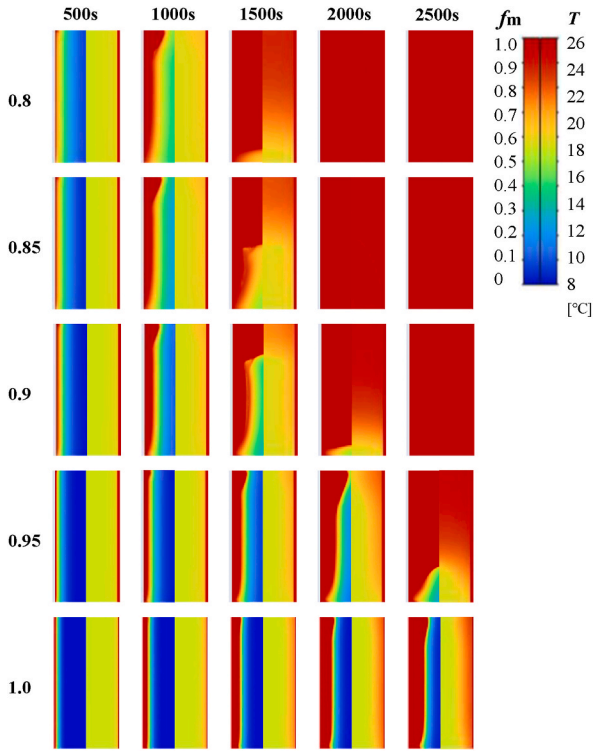

Fig. 7. Evolution of the liquid-fraction and temperature fields for different uniform porosity.

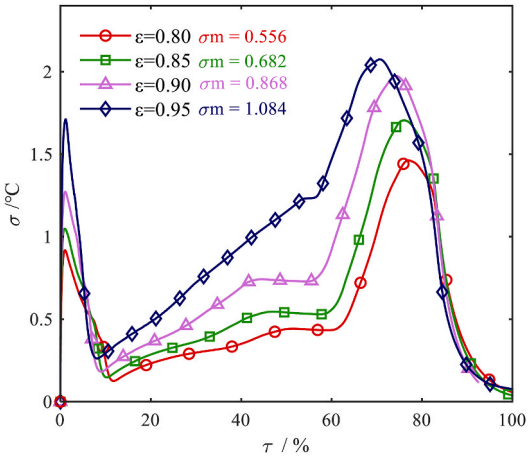

Fig. 8. Comparison of temperature uniformity for different uniform porosity.

where, $\overline{p_a}$ is the average pressure in the accumulator, which is taken as 10 MPa in this work, and V_{PCM} denotes the volume of the PCM volume in solid.

Fig. 9is plotted to illustrate the total melting time T_m, storage power P, and energy density E under different porosity configurations. As the porosity decreases from 0.95 to 0.8, the stored mechanical energy is slightly reduced, whereas the melting time is shortened, and the power increases from approximately 0.47 W to 0.72 W. Nevertheless, the energy density decreases because of the increased total mass, dropping gradually from 0.257 to 0.193. These results indicate that the thermal benefit of copper foam should be evaluated together with its mass penalty. A lower porosity shortens the melting time and increases storage power, but it also reduces the PCM volume and increases the copper-foam weight, which limits the improvement in energy density and power-to-weight performance.

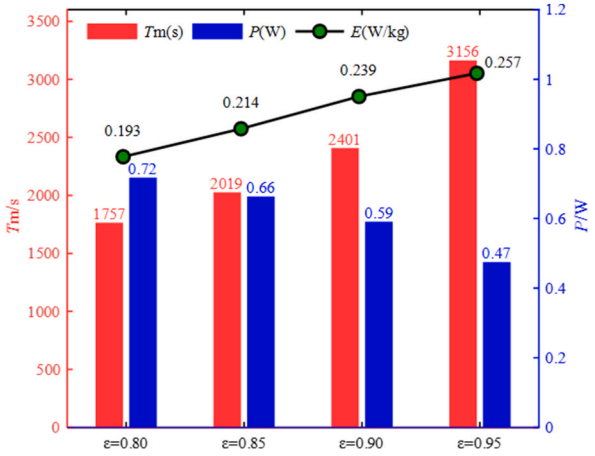

Fig. 9. Performance comparison for different uniform porosity.

4.2. *Effect of porosity gradient difference*

A graded-porosity configuration is proposed in this study to improve the utilization efficiency of copper foam. The graded-porosity configurations were selected by considering manufacturability, prototype size, structural stability, and system-level mass/buoyancy constraints. Since the porosity fabrication and measurement uncertainty of the copper foam manufactured by Kunshan Guangjiayuan New Material Co., Ltd. was approximately 0.01 in porosity, the minimum adjacent-layer porosity difference was set to 0.02 to ensure practical distinguishability and manufacturability. Meanwhile, the maximum outer diameter of the PCM chamber was limited to 100 mm according to the previous-generation prototype design, which constrained the number of radial layers; therefore, a four-layer structure was adopted to represent the radial gradient while avoiding deformation of overly thin annular copper-foam layers. Considering the mass penalty caused by the much higher density of copper than that of the PCM, the average porosity was fixed at 0.85. On this basis, gradient magnitudes of 0.02, 0.04, and 0.06 were used to represent weak, moderate, and strong gradients, corresponding to porosity ranges of 0.82–0.88. As shown schematically in Fig. 10, the two-dimensional cross-section illustrates a positive radial gradient structure (Gra.P), in which the porosity increases from the inner to the outer region, and a negative radial gradient structure (Gra.N), in which the porosity decreases radially outward. Table 3summarizes the distributions corresponding to different porosity increment rates (Gra.P1, Gra. P2, Gra. P3) and decrement rates (Gra.N1, Gra. N2, Gra. N3), while maintaining the same average porosity of 0.85. These configurations are used to investigate the influence of porosity gradients on the thermal response of the system.

As shown in Fig. 11, the temporal evolution of the liquid fraction (f_m) exhibits pronounced differences among the graded-porosity configurations. In the early melting stage, the melting rate of the positive-gradient group (Gra.P) is lower than that of the negative-gradient group (Gra.N), and a larger gradient difference leads to a slower melting rate. Meanwhile, the differences in melting rate among the configurations within the negative-gradient group are not significant, indicating that the negative-gradient distribution enhances the melting rate of the outer layer, but this enhancement becomes less pronounced as the outer-layer porosity decreases.

The negative-gradient group (Gra.N) shows a higher growth rate of the liquid fraction at the beginning of melting, and the corresponding curves exhibit a clear trend of first increasing and then decreasing. It is worth noting that, once the liquid fraction $f_m \geq 0.8$,

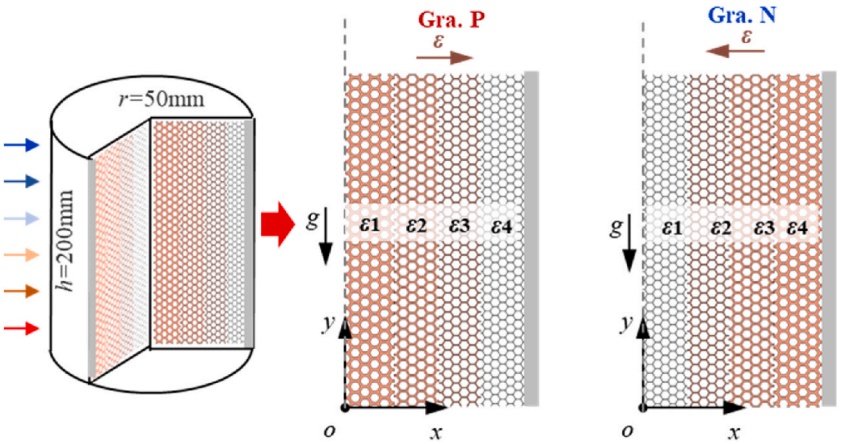

Fig. 10. Schematic distribution of graded-porosity configurations with different gradient magnitudes.

Table 3
Graded porosity configurations.

	ε1	ε2	ε3	ε4
Gra.P1	0.82	0.84	0.86	0.88
Gra.P2	0.79	0.83	0.87	0.91
Gra.P3	0.76	0.82	0.88	0.94
Gra.N1	0.88	0.86	0.84	0.82
Gra.N2	0.91	0.87	0.83	0.79
Gra.N3	0.94	0.88	0.82	0.76

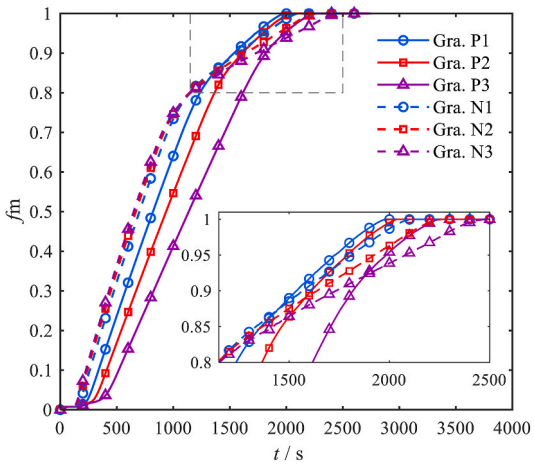

Fig. 11. Evolution of the liquid fraction for different porosity gradient magnitudes.

this growth rate drops markedly and gradually becomes lower than that of the positive-gradient group (Gra.P), ultimately leading to the longest total melting time for configuration Gra. N3, which has the largest gradient difference. The different liquid-fraction evolutions result from the redistribution of low- and high-porosity layers. In the negative-gradient cases, the low-porosity outer layer enhances early heat conduction near the heated wall, whereas in the positive-gradient cases the lower-porosity inner region becomes more effective when the melting front approaches the residual solid PCM.

Fig. 12 compares the total melting times for different positive and negative gradient magnitudes. For all gradient differences, the negative-gradient structures (Gra.N) exhibit longer complete melting times: the complete melting times of Gra. N1–N3 fall in the range of 2116–2497 s, which are all higher than the 1988–2248 s of Gra. P1–P3. It is noteworthy that, as the gradient difference increases, the discrepancy between the positive- and negative-gradient configurations gradually becomes larger, indicating that the regulatory effect of the porosity gradient distribution tends to saturate within a certain range. The influence of gradient magnitude is therefore not monotonic. A larger gradient strengthens the local contrast in thermal conductivity and permeability, but an excessive contrast may

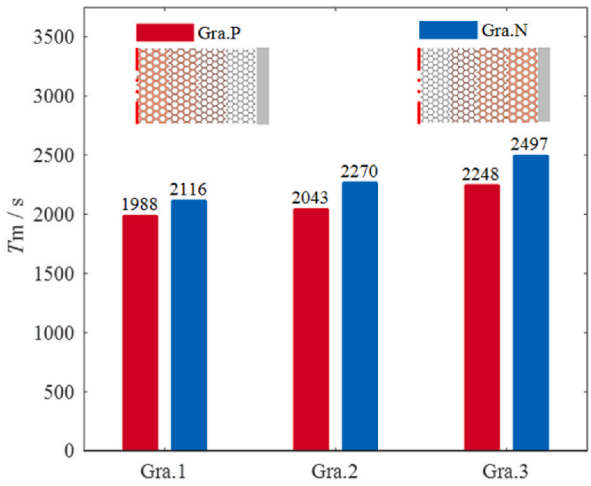

Fig. 12. Comparison of complete melting time for different porosity gradient magnitudes.

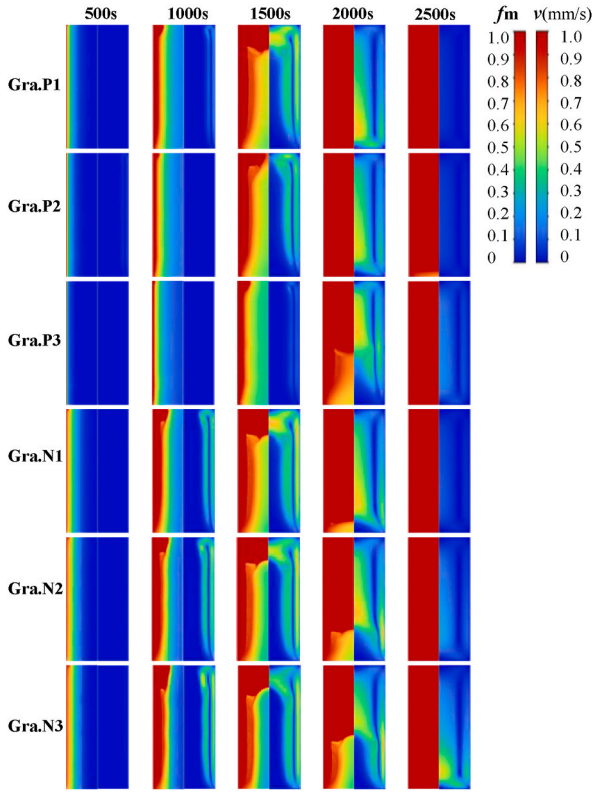

Fig. 13. Evolution of the liquid-fraction and velocity fields under different porosity gradient magnitude.

weaken heat-transfer continuity or liquid PCM circulation in part of the domain.

To elucidate the relationship between natural convection strength and the melting process, Fig. 13 depicts the evolution of the liquid fraction field (left) and the velocity field (right) for different porosity-gradient configurations. It can be seen that, for the negative-gradient cases, the melting front rapidly propagates inward at the early stage. This behavior is attributed to the lower porosity in the outer region, where melting is initiated earlier, while the higher porosity in the inner region provides stronger fluid permeability, thereby establishing a natural convection circulation that accelerates heat transfer toward the un-melted zone. In contrast, for the positive-gradient configurations, the velocity field advances downward earlier than in the negative-gradient cases during the later stage and ultimately completes the melting process first, indicating that the phase-change process of the inner PCM is more dependent on the low-porosity layer with a high specific surface area. The velocity fields further show that the role of natural convection varies with melting stage. Negative-gradient structures promote earlier liquid motion near the heated region, whereas positive-gradient structures maintain more effective heat transfer toward the inner residual solid PCM during the later stage, which explains their better overall melting performance.

To further quantify the natural-convection shown in Fig. 13, the maximum velocity of liquid PCM and the normalized melting progress was showed in Fig. 14. The normalized melting progress is defined as:

$$\tau = \frac{t}{t_m} \tag{20}$$

$$\overline{U}^{\tau}_{\max} = \int_0^1 U_{\max}(\tau) d\tau \tag{21}$$

$$U_{max,peak} = \max(U_{max}) \tag{22}$$

In this study, the early, middle, and late stages were defined as $0 < \tau \leq 0.4$, $0.4 < \tau \leq 0.8$, and $0.8 < \tau \leq 1$ respectively. It can be observed that the negative-gradient configurations develop stronger liquid motion at an earlier stage. In particular, Gra. N2 and Gra. N3 show a rapid increase in $U_{\max}$ before $\tau = 0.4$, whereas the positive-gradient configurations exhibit a delayed increase in $U_{\max}$. This indicates that the negative-gradient configurations promote the earlier establishment of buoyancy-driven circulation. The average value of $\overline{U}^{\tau}_{\max}$ for the negative-gradient group is $4.223 \times 10^{-4} \mathrm{m \cdot s^{-1}}$, which is 69.15% higher than that of the positive-gradient group ($2.497 \times 10^{-4} \mathrm{m \cdot s^{-1}}$). This confirms that the negative-gradient configurations generate stronger local liquid motion during the overall melting process. The difference is even more pronounced in the early stage. The early-stage average maximum velocity of the negative-

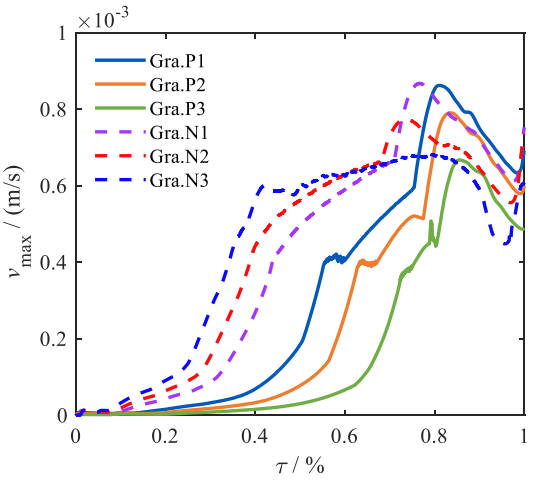

Fig. 14. Evolution of maximum velocity during the normalized melting process.

gradient group reaches $1.123 \times 10^{-4} \mathrm{m} \cdot \mathrm{s}^{-1}$. During the middle stage, the negative-gradient group still maintains a 127.26% higher average maximum velocity. In the late stage ($0.8 < \tau \leq 1$), the positive-gradient group shows a slightly higher average maximum velocity than the negative-gradient group, with an increase of 4.44%. For example, the late-stage average maximum velocity of Gra. P2 is 8.13% higher than that of Gra. N2, which is consistent with the velocity-field evolution shown in Fig. 13.

Fig. 15 illustrates the temporal variation of the temperature-uniformity index for different graded-porosity configurations. Overall, in the early melting stage dominated by heat conduction in the solid PCM, the negative-gradient configurations exhibit a higher effective thermal conductivity and thus a more uniform temperature distribution. The fact that they reach the minimum value earlier than the positive-gradient cases indicates that they enter the latent-heat absorption stage at an earlier time. In the later melting stage, however, the temperature distribution in the negative-gradient configurations becomes more non-uniform as the gradient magnitude increases, while the RMS value of the positive-gradient cases becomes lower than that of the negative-gradient ones. This suggests that, at this stage, placing the lower-porosity layers with higher specific surface area near the inner region provides an optimized heat-transfer pathway. During the melting process, the positive-gradient porosity configurations improve the time-averaged RMS temperature index by 39.3%, 40.9%, and 42.4%, respectively, compared with the uniform-porosity case, whereas the corresponding improvements for the negative-gradient configurations are 33.2%, 27.2%, and 15.4%.

The above analysis indicates that there exists a trade-off between the magnitude and direction of the porosity gradient and the melting efficiency. Therefore, the present study further evaluates the total melting time, storage power, weight, stored energy, and power density for different gradient directions and gradient magnitudes. As illustrated by the radar chart in Fig. 16, in comparison with the uniform porosity of 0.85, the negative-gradient configurations lead to inferior performance in all these metrics and thus should be adopted with caution. By contrast, all positive-gradient configurations exhibit advantages in terms of stored energy and self-weight. Among them, configuration Gra. P2, which has a moderate positive gradient difference, achieves the best overall performance.

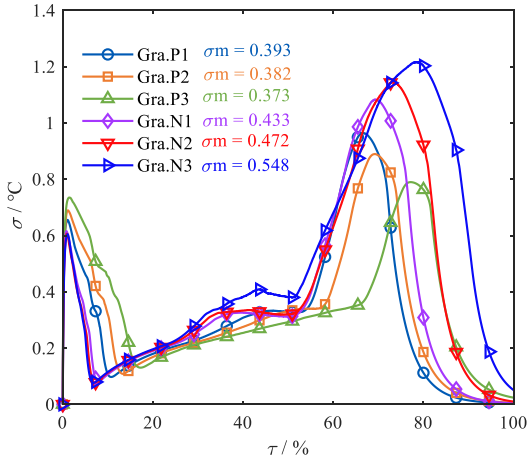

Fig. 15. Evolution of temperature uniformity for different porosity gradient magnitudes.

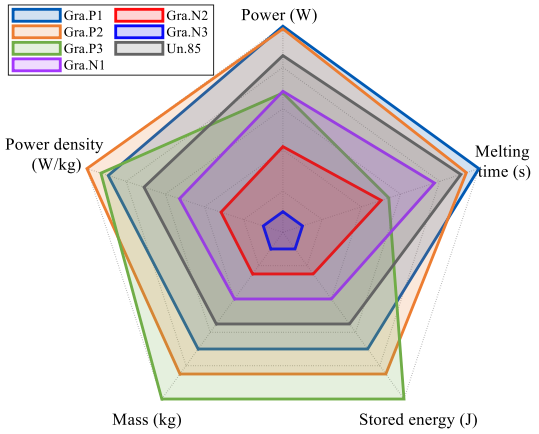

Fig. 16. Performance comparison for various porosity gradient magnitudes.

5. Conclusions

In this study, a radially graded-porosity copper foam strategy was proposed for the phase-change chamber of an ocean thermal energy conversion (OTEC) thermal engine. The objective was to enhance the melting response of the PCM while maintaining favorable energy-output density and power-to-weight performance. Through combined experimental validation and numerical analysis, the effects of pure PCM, uniform-porosity copper foam, and graded-porosity copper foam on liquid-fraction evolution, temperature uniformity, melting time, storage power, stored energy, and power density were systematically investigated. The main conclusions were summarized as follows.

(1) Embedding copper foam into the PCM significantly accelerated the melting process by providing a high-conductivity heat-transfer network. For the uniform-porosity configurations, decreasing porosity shortened the complete melting time, and the copper-foam configuration with a porosity of 0.8 reduced the complete melting time by 48.7% compared with pure PCM. However, the reduction in melting time gradually approached saturation as the porosity decreased. This is because lower porosity enhances conductive heat transfer through the copper skeleton but simultaneously increases flow resistance and suppresses the natural convection of liquid PCM.

(2) The negative-gradient porosity structures induced stronger liquid PCM motion in the early and middle stages, with the process-averaged maximum velocity being 69.15% higher than that of the positive-gradient group. However, this stronger early-stage convection did not translate into shorter complete melting time. The positive-gradient structures maintained slightly higher late-stage maximum velocity and provided a more favorable conduction–convection coupling for melting the remaining inner PCM, thereby achieving better overall melting performance.

(3) The graded-porosity structures improved the temperature uniformity of the PCM domain. Compared with the uniform-porosity case, the time-averaged RMS temperature index was improved by 33.2%, 27.2%, and 15.4% for the negative-gradient configurations, and by 39.3%, 40.9%, and 42.4% for the positive-gradient configurations, respectively. These results indicate that the positive-gradient arrangement is more effective in maintaining temperature uniformity over the full melting process, especially during the middle and late stages.

(4) It was noteworthy that, although a stronger heat-transfer enhancement can be achieved by increasing the copper-foam fraction, excessive copper content reduces the PCM volume and increases structural mass. Among the graded configurations, the moderate positive-gradient case achieved the best comprehensive performance because it balanced melting acceleration, temperature uniformity, energy storage capacity, and power-to-weight output.

In summary, this work provides a practical trade-off framework for designing high-power-density OTEC thermal engines by balancing heat-transfer enhancement, structural weight, and PCM volume. The proposed four-layer graded-porosity structure should be regarded as a prototype-level discrete implementation of the radial-gradient concept rather than a universal optimum for all scales. For full-scale OTEC thermal engines, radial thickness ratio, and continuous gradient function should be further optimized under coupled thermal, structural and buoyancy constraints. Moreover, although the present study focuses on the melting process because it directly determines the heat-absorption and mechanical-energy-storage performance, practical OTEC systems operate under repeated melting–solidification cycles. Future work should further evaluate solidification performance, thermal hysteresis and long-term stability of the PCM/copper-foam composite.

CRediT authorship contribution statement

Zengbao Zhang: Investigation, Methodology, Supervision, Writing – original draft. **Wenzhuo Shi:** Data curation, Investigation, Resources, Writing – original draft. **Sihan Zhang:** Validation, Writing – original draft. **Jingzhi Zhang:** Investigation, Methodology. **Bingzhen Wang:** Writing – review & editing. **Shizhen Li:** Funding acquisition, Investigation, Methodology.

Declaration of competing interest

The authors declare that they have no known competing financial interests or personal relationships that could have appeared to influence the work reported in this paper.

Acknowledgements

This work was financially supported by National Key Research and Development Program of China (Grant No.2023YFC2810000), Shandong Provincial Natural Science Foundation for Distinguished Young Scholars of Shandong Province (ZR2025QA22).

Data availability

Data will be made available on request.

References

[1] E. M., A New Concept for an Obstacle Avoidance System for the AUV "SLOCUM Glider" Operation Under Ice, OCEANS 2009-EUROPE, 2009, pp. 1–8.
[2] J. Yuh, G. Marani, D.R. Blidberg, Applications of marine robotic vehicles, INTEL SERV ROBOT 4 (2011) 221–231.
[3] E. Zereik, M. Bibuli, N. Mišković, P. Ridao, A. Pascoal, Challenges and future trends in marine robotics, Annu. Rev. Control 46 (2018) 350–368.
[4] Z. Yao, C. Yang, G. Muhammad, Q. Xia, Y. Chen, B. Chen, Thermal properties estimation of phase change material/copper foam composites for ocean thermal engine using inverse method, J. Energy Storage 126 (2025) 116999.
[5] Y. Yang, Y. Wang, Z. Ma, S. Wang, A thermal engine for underwater glider driven by ocean thermal energy, Appl. Therm. Eng. 99 (2016) 455–464.
[6] S. Wang, C. Xie, Y. Wang, L. Zhang, W. Jie, S.J. Hu, Harvesting of PEM fuel cell heat energy for a thermal engine in an underwater glider, J. Power Sources 169 (2007) 338–346.
[7] N. Şahan, M. Fois, H. Paksoy, Improving thermal conductivity phase change materials—A study of paraffin nanomagnetite composites, SOL ENERG MAT SOL C 137 (2015) 61–67.
[8] D. Singh, T. Kim, W. Zhao, W. Yu, D.M. France, Development of graphite foam infiltrated with MgCl2 for a latent heat based thermal energy storage (LHTES) system, RENEW ENERG 94 (2016) 660–667.
[9] S. Harikrishnan, S. Imran Hussain, A. Devaraju, P. Sivasamy, S. Kalaiselvam, Improved performance of a newly prepared nano-enhanced phase change material for solar energy storage, J. Mech. Sci. Technol. 31 (2017) 4903–4910.
[10] Z. Jiang, T. Ouyang, Y. Yang, L. Chen, X. Fan, Y. Chen, W. Li, Y. Fei, Thermal conductivity enhancement of phase change materials with form-stable carbon bonded carbon fiber network, MATER DESIGN 143 (2018) 177–184.
[11] S. Li, Y. Zhang, Z. Zhou, W. Shi, J. Zhang, B. Wang, Study on improving the storage efficiency of ocean thermal energy storage (OTES) unit by using fins, Case Stud. Therm. Eng. 37 (2022) 102262.
[12] C. Yang, Y. Xu, X. Xu, M. Bake, C. Wu, Y. Li, J. Yu, Melting performance analysis of finned metal foam thermal energy storage tube under steady rotation, Int. J. Heat Mass Tran. 226 (2024) 125458.
[13] N. Parsa, H. Abolghasemi, B. Kamkari, Experimental and numerical investigation of thermal performance enhancement in shell-and-tube latent heat storage systems: effects of fins, eccentricity, and shell geometry, J. Energy Storage 128 (2025) 117159.
[14] M. Aramesh, B. Shabani, Metal foam-phase change material composites for thermal energy storage: a review of performance parameters, Renew. Sustain. Energy Rev. 155 (2022) 111919.
[15] A. Chibani, M.A.N. Haddad, C. Boucetta, S. Merouani, R. Badji, F.L. Rashid, H.I. Mohammed, Simultaneous evaluation of PCM-metal foam (polyethylene glycol 1500-AlSi10Mg) composite with porous structures fabricated via additive manufacturing: the influence of porosity and pore size, Appl. Therm. Eng. 277 (2025) 126988.
[16] H.I. Mohammed, Discharge improvement of a phase change material-air-based thermal energy storage unit for space heating applications using metal foams in the air sides, HEAT TRANSF 51 (2022) 3830–3852.
[17] P.T. Sardari, H.I. Mohammed, J.M. Mahdi, M. Ghalambaz, M. Gillott, G.S. Walker, D. Grant, D. Giddings, Localized heating element distribution in composite metal foam-phase change material: fourier's law and creeping flow effects, INT J ENERG RES 45 (2021) 13380–13396.
[18] J.M. Mahdi, H.I. Mohammed, P. Talebizadehsardari, M. Ghalambaz, H. Sh Majdi, A. Khan, W. Yaïci, D. Giddings, Simultaneous and consecutive charging and discharging of a PCM-based domestic air heater with metal foam, Appl. Therm. Eng. 197 (2021) 117408.
[19] P. Talebizadehsardari, H.I. Mohammed, J.M. Mahdi, M. Gillott, G.S. Walker, D. Grant, D. Giddings, Effect of airflow channel arrangement on the discharge of a composite metal foam-phase change material heat exchanger, INT J ENERG RES 45 (2020) 2593–2609.
[20] H.I. Mohammed, P.T. Sardari, D. Giddings, Multiphase flow and boiling heat transfer modelling of nanofluids in horizontal tubes embedded in a metal foam, Int. J. Therm. Sci. 146 (2019) 106099.
[21] X. Wei, N. Zhang, Z. Zhang, X. Cao, Y. Yuan, Melting evaluation of phase change materials impregnated into cascaded metal foams with regionalized enhancement, J. Therm. Sci. 34 (2025) 223–241.
[22] Z. Zhang, X. He, Three-dimensional numerical study on solid - liquid phase change within open-celled aluminum foam with porosity gradient, Appl. Therm. Eng. 113 (2017) 298–308.
[23] T. Si, W. Cui, T. Ma, L. Lu, Q. Wang, Numerical investigation on thermal performance of phase change materials embedded in functionally graded metal foam, J. Energy Storage 81 (2024) 15.
[24] C. Zhao, M. Opolot, M. Liu, F. Bruno, S. Mancin, K. Hooman, Numerical study of melting performance enhancement for PCM in an annular enclosure with internal-external fins and metal foams, Int. J. Heat Mass Tran. 150 (2020) 119348.
[25] B. Buonomo, M. Rita Golia, O. Manca, S. Nardini, A review on thermal energy storage with phase change materials enhanced by metal foams, Therm. Sci. Eng. Prog. 53 (2024) 102732.
[26] K. Venkateshwar, S.H. Tasnim, H. Simha, S. Mahmud, Effect of spatially varying morphologies of metal foams on phase change process, Therm. Sci. Eng. Prog. 19 (2020) 100667.
[27] K. Lafdi, O. Mesalhy, S. Shaikh, Experimental study on the influence of foam porosity and pore size on the melting of phase change materials, J. Appl. Phys. 102 (2007) 6.

[28] F. Zhu, X. Hu, X. Wang, C. Zhang, X. Gong, Experimental and numerical investigation of the melting process of aluminum foam/paraffin composite with low porosity, Numer. Heat Transf. A Appl. 77 (2020) 998–1013.
[29] G. Muhammad, Z. Yao, Y. Chen, Q. Xia, C. Yang, Experimental investigation on thermal performance of phase change materials–metal foam composites in ocean thermal engine, Case Stud. Therm. Eng. 60 (2024) 104693.
[30] N. Zhang, Z. Zhang, X. Wei, Y. Du, H. Köten, Y. Yuan, Multiple optimization design on gradient porosity of copper foam in phase change materials based on genetic algorithm, Int. J. Heat Mass Tran. 241 (2025) 126764.
[31] A. Bhattacharya, V.V. Calmidi, R.L. Mahajan, Thermophysical properties of high porosity metal foams, Int. J. Heat Mass Tran. 45 (2002) 1017–1031.
[32] A. Pourakabar, A.A. Rabienataj Darzi, Enhancement of phase change rate of PCM in cylindrical thermal energy storage, Appl. Therm. Eng. 150 (2019) 132–142.
[33] Y. Li, X. Huang, T. Lai, Y. Wu, X. Yang, B. Sundén, Thermal characteristics of conical heat storage tank filled by metal foam: optimization by response surface analysis, Int. J. Therm. Sci. 208 (2025) 109450.
[34] X. Gao, P. Wei, J. Yu, X. Huang, X. Yang, B. Sundén, Design and assessments on graded metal foam in heat storage tank: an experimental and numerical study, INT COMMUN HEAT MASS 146 (2023) 106902.
[35] G. Wang, Y. Yang, S. Wang, Ocean thermal energy application technologies for unmanned underwater vehicles: a comprehensive review, APPL ENERG 278 (2020) 115752.